aerospace

MDPI

Article

Thermal Environment for Lunar Orbiting Spacecraft Based on Non-Uniform Planetary Infrared Radiation Model

Xinqi Li *, Liying Tan, Jing Ma and Xuemin Qian

School of Astronautics, Harbin Institute of Technology, Harbin 150001, China
* Correspondence: 23b921022@stu.hit.edu.cn

Abstract

Accurate computation of external heat flux is critical for spacecraft thermal analysis and thermal control system design. The traditional method, which adopted the uniform planetary infrared radiation model (UPIRM), is inadequate for lunar orbital missions due to the extreme planetary surface temperature variations. This study proposes an external heat flux calculation method for lunar orbits by integrating a non-uniform lunar surface temperature model derived from Lunar Reconnaissance Orbiter (LRO) Diviner radiometric data. Specifically, the lunar surface temperature data were first fitted as functions of latitude (ψ) and position angles (ζ) through data regression analysis. Then, a comprehensive mathematical framework is established to analyze solar radiation, lunar albedo, and lunar infrared radiation components, incorporating orbital parameters such as beta angle (β), orbital inclination (i) and so on. Coordinate transformations and numerical integration techniques are employed to evaluate heat flux distributions across cuboidal orbiter surfaces. It is found that the lunar infrared radiation heat flux manifests pronounced fluctuation, peaking at 1023 W/m^2 near the lunar noon region while plummeting to 20 W/m^2 near the midnight region under the orbital parameters investigated in this study. This study demonstrates the essential role of the non-uniform planetary infrared radiation model (NUPIRM) in enhancing prediction accuracy by contrast, offering foundational references for thermal management in future lunar and deep-space exploration spacecraft.

Keywords: external heat flux; lunar orbit; lunar infrared radiation heat flux; spacecraft thermal analysis; non-uniform planetary radiation model

check for updates

Academic Editor: Hyun-Ung Oh

Received: 5 June 2025
Revised: 15 August 2025
Accepted: 18 August 2025
Published: 19 August 2025

Citation: Li, X.; Tan, L.; Ma, J.; Qian, X. Thermal Environment for Lunar Orbiting Spacecraft Based on Non-Uniform Planetary Infrared Radiation Model. *Aerospace* **2025**, *12*, 737. https://doi.org/10.3390/aerospace12080737

Copyright: © 2025 by the authors. Licensee MDPI, Basel, Switzerland. This article is an open access article distributed under the terms and conditions of the Creative Commons Attribution (CC BY) license (https://creativecommons.org/licenses/by/4.0/).

1. Introduction

Spacecraft are exposed to extremely harsh space thermal environments during operations. Maintaining onboard instruments within safe temperature ranges through thermal control systems is a prerequisite for mission completion [1,2]. Consequently, thermal analysis and thermal vacuum experiments, which serve as key technologies for the design and verification of spacecraft thermal control systems, have thus become important components of the spacecraft development process [3–5]. Among them, calculating the external heat flux based on spacecraft orbital information is a fundamental aspect [6–9].

Currently, the calculation methods for external heat flux of Earth orbit have been relatively mature [10]. The heat flux is typically evaluated through separate calculations of three distinct components: solar radiation heat flux, Earth-reflected heat flux, and Earth infrared radiation heat flux, which are subsequently aggregated. The solar radiation heat flux primarily depends on the solar constant (S) and beta angle (β, which is defined as the angle between the solar vector and orbital plane). The calculation of the Earth-reflected

heat flux and Earth infrared radiation heat flux relies on Earth's albedo, infrared radiation intensity, and orbital parameters, utilizing numerical integration methods for precise evaluation. During the thermal control system design, simulation verification, and experimental validation phases, it is customary to consider the maximum and minimum external heat flux boundaries throughout the entire orbital cycle as the extreme on-orbit thermal environments to verify the reliability of the thermal control system. Selvadurai et al. [11] conducted numerical simulations to investigate the effectiveness of passive thermal control techniques for infrared imaging instruments on Earth-orbiting satellites under two extreme cases. For the worst cold condition, the albedo constant of the Earth is set to 0.2 and the infrared flux is equal to 230 W/m^2, while for the worst hot condition, the corresponding values were configured as 0.32 and 250 W/m^2. Reference [6] analyzed the external heat flux of a microsatellite under varying β, identified the optimal heat dissipation surface location and extreme conditions, and validated the thermal control system through experimental testing. Garzon et al. [12] established a simplified multi-node thermal analysis model for 3U satellites and investigated the effects of contact conductances on the temperature distribution when $\beta \in [0^\circ, 75^\circ]$. These methodologies provide critical references for establishing thermal design verification protocols and ensuring spacecraft thermal stability in complex orbital environments. In addition, certain specialized studies, such as the deformation analysis of spacecraft support structures during mission cycles, necessitate consideration of external heat flux variations throughout the entire orbital period [7,13].

Furthermore, with the continuous advancement of global space exploration programs, space missions have progressively expanded toward lunar exploration, placing new demands on the thermal analysis of lunar-orbiting spacecraft, particularly in the computation of external heat fluxes [14]. Compared to Earth orbits, the thermal environment in lunar orbits is more extreme and complex, primarily due to differences in planetary infrared radiation characteristics. This distinction arises from the absence of the atmosphere around the Moon, which allows drastic temperature variations on the lunar surface in response to solar radiation. Due to the Moon's 28-Earth-day diurnal cycle (14-day lunar day and 14-day lunar night), prolonged solar exposure elevates daytime surface temperatures beyond 120 °C (393 K), while in topographically unique regions and during the lunar night without solar radiation, surface temperatures plunge below −170 °C (103 K) [15]. This pronounced spatial and temporal inhomogeneity in lunar surface temperature induces significant fluctuations in infrared radiative heat flux over an orbital period.

To enhance the precision of external heat flux calculations for lunar orbits, it is imperative to account for the influence of non-uniform lunar surface temperature models on orbital infrared heat flux dynamics [16]. The studies on the temperature distribution characteristics of the lunar surface began in the early 20th century. With the implementation of lunar exploration programs, the temperature data acquisition methods evolved from ground-based observations to orbital measurements and direct in situ measurements. In 2009, NASA launched the Lunar Reconnaissance Orbiter (LRO), whose Diviner lunar radiometer experiment began collecting radiation data in visible and infrared spectra to derive lunar surface temperatures [17]. In 2017, Hayne [18] utilized LRO Diviner datasets to establish and refine a numerical model for lunar surface temperature, conducting detailed analyses of diurnal temperature variations, seasonal fluctuations, and thermal behavior. These datasets provide critical foundations for evaluating lunar surface temperature inhomogeneity and remain the most widely adopted lunar thermal model in current applications. In response to growing interest in lunar polar exploration missions and the development of water ice resources, recent studies have further advanced numerical simulations and experimental validations of polar thermal environments [19,20]. This progression in measurement

methodologies and modeling techniques significantly enhances the fidelity of spacecraft thermal analysis for future lunar missions.

However, existing methodologies for lunar infrared radiative heat flux calculations often rely on simplified assumptions. These approaches typically neglect actual lunar thermal properties in radiative heat transfer predictions. Yi employed a uniform planetary infrared radiation model (UPIRM), whereby all lunar surface locations were assumed to uniformly emit the total solar radiation absorbed by the whole Moon [8]. Separately, Li postulated that each infinitesimal surface element on the sunlit hemisphere maintains energy balance between absorbed solar flux and emitted infrared radiation under the energy conservation principle, asserting that the infrared radiation intensity of any lunar surface element equals its absorbed solar radiation [14]. As lunar surface temperature modeling was launched, subsequent studies began incorporating the effects of temperature inhomogeneity into lunar orbital heat flux calculations. For instance, in the Lunar Laser Communication Demonstration (LLCD) project and China's lunar exploration missions, researchers have conducted thermal management design and verification for spacecraft by integrating orbital parameters with lunar surface temperature distribution characteristics [20–22]. Nevertheless, the thermal flux calculation methodologies employed in these studies have not been comprehensively elucidated.

In summary, the non-uniform temperature distribution across the lunar surface significantly affects the thermal environment of lunar orbiters, while related published computational methods and systematic analyses remain insufficient. To address this issue, this study establishes a non-uniform planetary infrared radiation model (NUPIRM) for the lunar surface based on the lunar surface temperature model proposed in Ref. [18]. Three coordinate systems—the lunar-centric, orbital, and spacecraft body-fixed frames—are established to calculate solar radiation, lunar albedo, and lunar infrared radiation heat fluxes. Coordinate transformation algorithms and numerical integration techniques are applied to characterize heat flux variations along a Keplerian elliptical orbit with semi-major axis a = 100 km and eccentricity e = 0.05. The analysis explicitly quantifies the influence of β on external heat flux and contrasts the results of the proposed NUPIRM with UPIRM.

The remainder of this paper is organized as follows: Section 2 details the establishment of coordinate systems, vector transformation methods, and numerical integration algorithms. Section 3 analyzes the geometric relationship between orbital parameters and β, presents computational results of orbital heat flux under varying β, and compares discrepancies between the NUPIRM and UPIRM. Section 4 concludes the study, discusses limitations, and outlines future research directions.

2. Mathematical Model

2.1. Coordinate System Establishment and Transformation

The orbital external heat flux experienced by a spacecraft is determined by its orbital parameters, flight attitude, and relative position to the Sun. The spatial position of a spacecraft is conventionally described using six classical orbital parameters: semi-major axis of the Keplerian elliptical orbit (a), eccentricity of the elliptical orbit (e), orbital inclination (i), argument of perilune (ω), longitude of ascending node (Ω), and true anomaly (φ). The angle β, which decides the spacecraft's attitude and represents the geometric relationship between orbital plane and solar direction, critically influences thermal environmental conditions. To enable systematic calculation of spatial heat flux across any orbital position during the mission cycle, two coordinate systems are established: a selenocentric coordinate system $S_m(O_m, X_m, Y_m, Z_m)$(Figure 1) and an orbital coordinate system $S_o(O_o, X_o, Y_o, Z_o)$(Figure 2). In S_m: X-axis is directed toward the intersection of the prime meridian and lunar equator, Z-axis is aligned with the lunar north pole, and the Y-axis is

determined by the right-handed Cartesian convention. In S_o: X-axis is oriented along the orbital ellipse semi-major axis, Z-axis is perpendicular to the orbital plane, and Y-axis is also determined by the right-handed Cartesian convention.

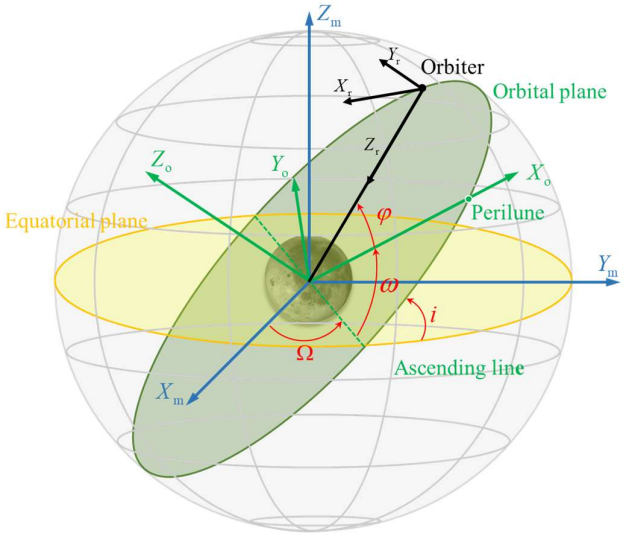


Figure 1. The geometric relationship among orbital parameters, lunar equatorial plane, orbital plane, selenocentric coordinate system, and orbital coordinate system.

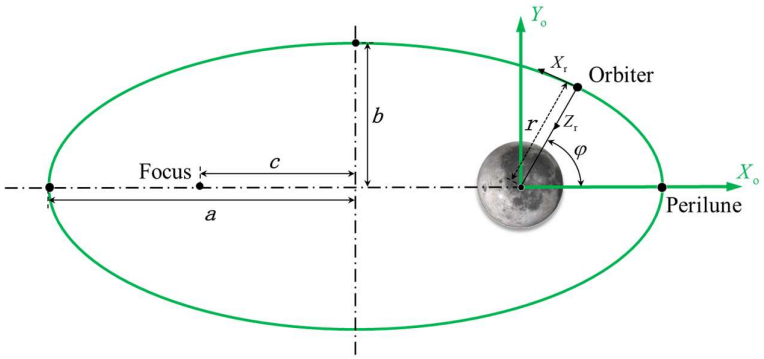


Figure 2. The orbital coordinate system S_o.

The position of the orbiter within its orbital cycle is characterized by φ. Utilizing Kepler's third law and the parametric equations of an elliptical orbit, the distance from the orbiter to the lunar center can be expressed as:

$$r = \frac{p}{1 + e\cos\varphi} \tag{1}$$

where $p = a(1 - e^2)$ denotes the semi-latus rectum of the elliptical orbit.

The positions of the orbiter in the coordinate system S_o are thus represented as:

$$[x, y, z]_o = [r\cos\varphi, r\sin\varphi, 0]_o \tag{2}$$

To establish the coordinate transformation from the coordinate system S_o to S_m, a three-step rotation sequence is implemented: (1) the orbital plane is rotated $-\Omega$ around the Z-axis of S_m, aligning the ascending line with the X-axis of S_m; (2) the orbital plane is rotated $-i$ around the X-axis, aligning the orbital plane's normal vector with the Z-axis; and (3) the orbital plane is rotated $-\omega$ around the Z-axis, aligning the direction of perilune with the positive X-axis. The coordinate transformation matrix is expressed as:

$$[x, y, z]_m^T = T_{o\text{-}m}[x, y, z]_o^T \tag{3}$$

$$\begin{aligned} \mathrm{T}_{\text{o-m}} &= R_z(-\Omega)R_x(-i)R_z(-\omega) \\ &= \begin{bmatrix} \cos\Omega\cos\omega - \sin\Omega\cos i\sin\omega & -\cos\Omega\sin\omega - \sin\Omega\cos\omega\cos i & \sin\Omega\sin i \\ \sin\Omega\cos\omega + \cos\Omega\cos i\sin\omega & -\sin\Omega\sin\omega + \cos\Omega\cos i\cos\omega & -\cos\Omega\sin i \\ \sin\omega\sin i & \cos\omega\sin i & \cos i \end{bmatrix} \end{aligned} \tag{4}$$

The flight attitudes of the orbiter encompass two operational modes with four distinct orientations, determined by β. The sign convention of β assigns a positive value when the solar vector aligns with the orbital normal vector and a negative value when opposing it. The forward flight mode is adopted when β resides within the range $|\beta| \leq \pi/4$, while the side flight mode is adopted if $|\beta| > \pi/4$. Table 1 shows the flight attitude and orientation of the surfaces of the orbiter.

Table 1. The flight attitude and orientation of the surfaces of the orbiter.

Mode/ Condition	**Forward Flight/ +Y Surface Sun-Avoided**		**Side Flight/ +X Surface Sun-Avoided**	
Attitude	Forward flight	Reverse flight	Side-swing forward	Side-swing reverse
X-axis of S_r	+X-axis points to the direction of velocity	−X-axis points to the direction of velocity	Perpendicular to the orbital plane	
Y-axis of S_r	Perpendicular to the orbital plane		+Y-axis points to the direction of velocity	–Y-axis points to the direction of velocity
Z-axis of S_r	+Z-axis points to the lunar			

The orbiter's body-fixed coordinate system $S_\mathrm{r}(O_\mathrm{r},\ X_\mathrm{r},\ Y_\mathrm{r},\ Z_\mathrm{r})$ is established with reference to the axis orientations of its forward flight attitude. Within the coordinate system S_r, the outward normal vectors of the orbiter's +X, +Y, and +Z surfaces are defined. To complete the vector calculations, these vectors are subsequently transformed into S_m through coordinate rotations. In S_o, the outward normal vectors of the +X, +Y, and +Z surfaces for forward flight are expressed as:

$$\vec{n}_{+x} = [-r\sin\varphi, r\cos\varphi, 0]_\mathrm{o} \tag{5}$$

$$\vec{n}_{+y} = [0, 0, r]_\mathrm{o} \tag{6}$$

$$\vec{n}_{+z} = [-r\cos\varphi, -r\sin\varphi, 0]_\mathrm{o} \tag{7}$$

In a coordinate system S_m, the position of a lunar surface differential element ds is parameterized by its zenith angle θ and azimuth angle ϕ, then the vector $\vec{n}_1$ pointing from the lunar center to ds is denoted as:

$$\vec{n}_1 = [R\cos\theta, R\sin\theta\sin\phi, R\sin\theta\cos\phi]_\mathrm{m} \tag{8}$$

where R is the lunar radius with R = 1,737,500 m.

To facilitate the definition of integration bounds, a coordinate transformation is implemented in S_m by rotating both the lunar sphere and the orbital plane until the line connecting the lunar center and the orbiter aligns with the positive X-axis. The resulting positional relationships among the transformed orbiter surface, orbital plane, solar vector, and lunar surface differential elements ds are schematically depicted in Figure 3. The transformation matrix is defined as:

$$\mathrm{T}_{\text{m-m}}{}' = R_z(\Omega)R_x(i)R_z(\omega+\varphi) \tag{9}$$

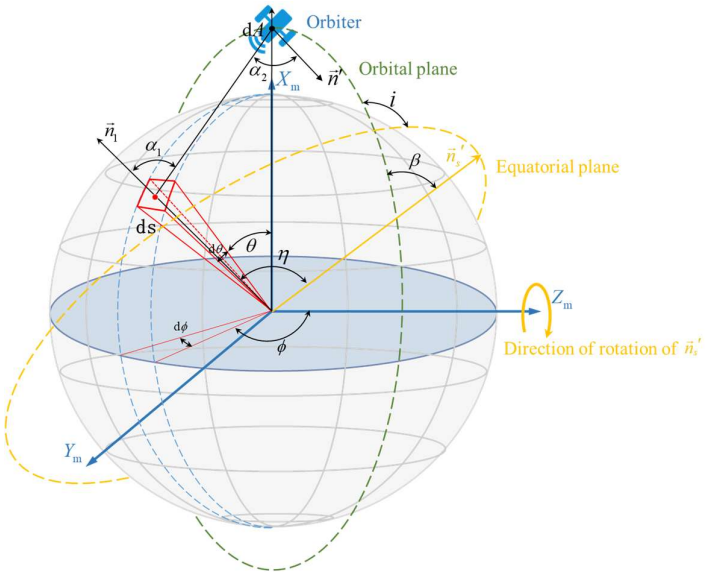


Figure 3. Geometric relationships among the lunar surface element d*s*, orbiter, orbital plane, solar vector $\vec{n}_s'$, and the equatorial plane after coordinate rotation.

Following the transformation, the outer normal vectors of +X, +Y, and +Z surfaces in coordinate system S_m are denoted as:

$$\vec{n}_{+x}{}' = \mathrm{T_{m\text{-}m}}'\mathrm{T_{o\text{-}m}}[-r\sin\varphi, r\cos\varphi, 0]_o^{\mathrm{T}} = [0, r, 0]_m \tag{10}$$

$$\vec{n}_{+y}{}' = \mathrm{T_{m\text{-}m}}'\mathrm{T_{o\text{-}m}}[0, 0, r]_o^{\mathrm{T}} = [0, 0, r]_m \tag{11}$$

$$\vec{n}_{+z}{}' = \mathrm{T_{m\text{-}m}}'\mathrm{T_{o\text{-}m}}[-r\cos\varphi, -r\sin\varphi, 0]_o^{\mathrm{T}} = [-r, 0, 0]_m \tag{12}$$

This transformation enhances computational efficiency, particularly for heat flux analysis on irregular surfaces of the orbiter. As both solar radiation heat flux and lunar albedo heat flux depend on the relative positions of the Sun and orbiter, the solar vector is also rotated accordingly:

$$\vec{n}_s' = \mathrm{T_{m\text{-}m}}'[x_s, y_s, z_s]_m^{\mathrm{T}} \tag{13}$$

This study employs the aforementioned vector and coordinate transformation to establish a framework and calculate the external heat flux distribution across the exterior surfaces of a cuboidal lunar orbiter.

2.2. Model Parameters and Assumptions

For this study, the solar constant S = 1354 W/m^2, and the other model parameters reference the orbital parameters of the lunar polar exploration mission, specifically $a = 100$ km, $e = 0.05$, $\omega = 270°$. The angle β exhibits a periodic variation range of $[-i - \mu,\ i + \mu]$ during the lunar revolution, where $\mu = 6.68°$ represents the effective obliquity between the ecliptic plane and the lunar equator. This inclination μ results from the superposition of two components: (1) the 5.14° is the angle between the Earth's ecliptic and the lunar equator; (2) another 1.54° is the angle between the lunar rotational axis and the outer normal vector of the ecliptic plane. This study is based on the lunar surface temperature distribution model under the presumption that the sun is directly irradiating the lunar equator, thereby the theoretical range of β is $[-i,\ i]$. By neglecting the Moon's orbital progression, β is treated as constant within a single orbital period of the orbiter. After determining the aforementioned parameters, Ω is found to have no measurable impact on the heat flux distribution. For computational consistency, Ω is fixed at 90° throughout the analysis.

Consequently, in the orbital period, under different conditions of β and i, the solar vector Expression (13) can be represented as:

$$\vec{n}_s' = d_{\mathrm{ms}} \mathrm{T_{m\text{-}m}}' [-\sin\beta/\tan i, \sqrt{\cos\beta^2 - (\sin\beta/\tan i)^2}, -\sin\beta]_{\mathrm{m}}^{\mathrm{T}} \tag{14}$$

where d_{ms} is the distance between the Moon and the Sun with $d_{\mathrm{ms}} = 1.496 \times 10^{11}$m.

2.3. Solar Radiation Heat Flux

The calculation of solar radiation heat flux q_{s} over an orbital period begins with determining the true anomalies φ_{in} and φ_{out} at which the orbiter enters and exits the lunar shadow. Geometrically, the lunar shadow is modeled as a conical region with its base formed by the Moon's cross-section normal to the solar vector, as illustrated in Figure 4. The geometric equations are:

$$F(x,y,z)_{\mathrm{o}} = (\left|\vec{n}_{\mathrm{s}}'\right| + d_{ym} - \left|\vec{v}\right| \cos a) \tan\sigma - d = 0 \tag{15}$$

$$d_{ym} = R d_{\mathrm{ms}} / (R_{\mathrm{s}} - R) \tag{16}$$

$$\sigma = \arcsin(R/d_{ym}) \tag{17}$$

where d_{ym} is the height of the conical region; $\vec{v}$ is the vector pointing from the orbiter to the solar; a is the angle between $\vec{v}$ and $\vec{n}_{\mathrm{s}}'$; σ is the angle between the generatrix and the height of the conical; d is the distance from the orbiter to $\vec{n}_{\mathrm{s}}'$; R_{s} is the solar radius with $R_{\mathrm{s}} = 1.39 \times 10^9$m.

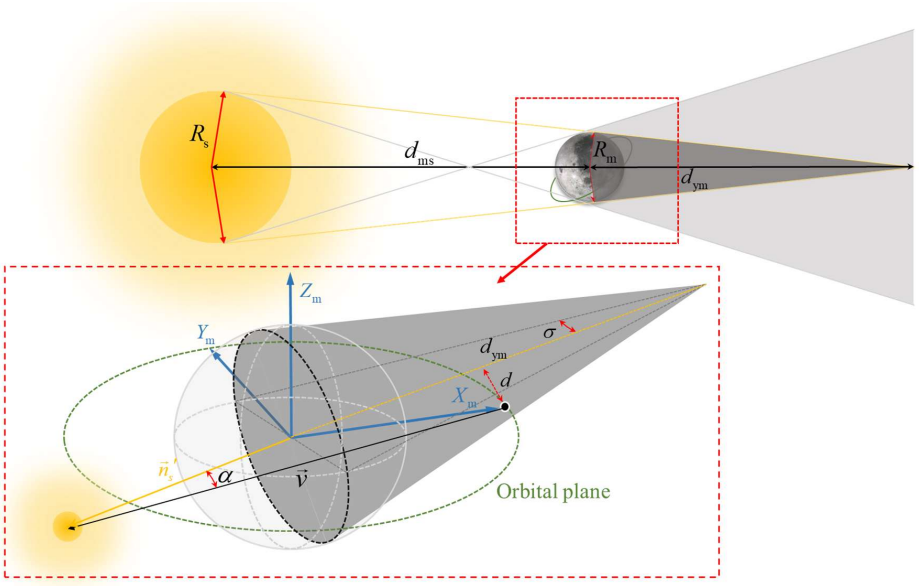


Figure 4. Diagram of calculation for φ_{in} and φ_{out}.

The parameter d and the component $\left|\vec{v}\right| \cos a$ are geometrically related through:

$$d = \left|\vec{v}\right| \sin a = \sqrt{\left|\vec{v}\right|^2 - \left(\left|\vec{v}\right| \cos a\right)^2} = \sqrt{\left|\vec{v}\right|^2 - \left(\frac{\vec{n}_s' \cdot \vec{v}}{\left|\vec{n}_s'\right|}\right)^2} \tag{18}$$

The angle φ within the coordinate transformation matrix $\mathrm{T_{m\text{-}m}}'$ of the vector $\vec{n}_s'$ is numerically resolved through Equation (15). However, two special cases exist: (1) no

solution exists for the equation, which indicates that the spacecraft does not enter the lunar shadow region during its orbital period under the given orbital parameters; (2) multiple solutions may exist due to the trigonometric functions and vector modulus forms of the unknown variable φ in the equation system. Additional conditions must be introduced to filter valid solutions. As shown in Figure 4, the spacecraft satisfies the following criterion when in the lunar shadow region:

$$\vec{n}_{\mathrm{s}}{}' \cdot [r, 0, 0] < 0 \tag{19}$$

The values of φ_{in} and φ_{out} are calculated via Equations (15)–(18). When the orbiter resides within the lunar shadow ($\varphi \in [\varphi_{\mathrm{in}}, \varphi_{\mathrm{out}}]$), $q_{\mathrm{s}} = 0$. During sunlit phases ($\varphi \notin [\varphi_{\mathrm{in}}, \varphi_{\mathrm{out}}]$), the flux q_{s} on each surface is expressed as:

$$q_{\mathrm{s,k}} = S\max(\cos\beta_k, 0)\left(k = X^+, X^-, Y^+, Y^-, Z^+, Z^-\right) \tag{20}$$

where β_k is the angle between the outer normal vector of orbiter surface k and the vector $\vec{n}_s'$.

For the $+Y$ surface, the angle β_{Y+} remains equivalent to β throughout the orbital period. Other angles are computed via the cosine law. Taking the $+X$ surface as an example:

$$\cos\beta_{\mathrm{X+}} = \frac{\vec{n}_s' \cdot \vec{n}_{+X}'}{\left|\vec{n}_s'\right| \cdot \left|\vec{n}_{+X}'\right|} \tag{21}$$

2.4. Lunar Albedo Heat Flux

It is assumed that the lunar surface is a Lambertian reflector during the lunar albedo heat flux calculation. The albedo heat flux from the surface element ds is expressed as:

$$q_{r-\mathrm{ds}} = \rho S\max(0, \cos\eta) \tag{22}$$

$$\eta = \arccos\frac{\vec{n}_s' \cdot \vec{n}_1}{\left|\vec{n}_s'\right|\left|\vec{n}_1\right|} \tag{23}$$

where η denotes the angle between $\vec{n}_s'$ and the vector connecting the lunar center to ds; ρ is the albedo of the lunar surface with $\rho = 0.14$ [23].

Following Lambert's cosine law, the heat flux q_{r} received by the surface element dA of the spacecraft is formulated as:

$$q_{\mathrm{r}} = \int_0^{2\pi}\int_0^{\arccos(R/r)} \frac{q_{r\text{-ds}}\cos\alpha_1\max(0,\cos\alpha_2)}{\pi L^2} R^2\sin\theta \mathrm{d}\theta\mathrm{d}\phi \tag{24}$$

$$X_{\text{ds-d}A} = \frac{\cos\alpha_1\max(0,\cos\alpha_2)}{\pi L^2} R^2\sin\theta\mathrm{d}\theta\mathrm{d}\phi \tag{25}$$

where $X_{\text{ds-d}A}$ is the view factor from ds to dA; L denotes the distance between ds and dA; both the integral bounds for ϕ and θ are determined by the observable lunar surface area from the orbiter.

2.5. Lunar Infrared Radiation Heat Flux

The lunar infrared radiation heat flux q_{e} is expressed as:

$$q_{\mathrm{e}} = \int_0^{2\pi}\int_0^{\arccos[R/r]} E_{\mathrm{ds}}\frac{\cos\alpha_1\max(0,\cos\alpha_2)}{\pi L^2} R^2\sin\theta\mathrm{d}\theta\mathrm{d}\phi \tag{26}$$

where E_{ds} is the radiative intensity of ds; α_1 is the angle between $\vec{n}_1$ and the connecting line from ds to dA; α_2 is the angle between the surface outer normal vector of dA and the connecting line from ds to dA.

Conventional approaches for calculating the radiative intensity E_{ds} of lunar surface elements often presume that the lunar surface is a uniform radiative surface, where the thermal equilibrium is maintained through uniform emission of absorbed solar energy. This yields:

$$E_{ds} = (1 - \rho)S/4 \tag{27}$$

This study delves into the influence of the non-uniform lunar surface temperature on the infrared radiation heat flux. We establish the relationship between lunar surface temperature and the solar vector through polynomial regression analysis of existing data. Then compute E_{ds} using the Stefan–Boltzmann law:

$$E_{ds} = \sigma \alpha {T_{ds}}^4 \tag{28}$$

where σ is the Stefan–Boltzmann constant with $\sigma = 5.67 \times 10^{-8} \mathrm{W}/\left(\mathrm{m}^2 \cdot \mathrm{K}^4\right)$; α is the emissivity of the lunar surface with $\alpha = 1 - \rho$; T_{ds} is the temperature of ds.

A piecewise polynomial regression method was employed to fit temperature–latitude–local time relationships derived from the literature [23]. When sunlight directly illuminates the lunar equator, surface temperatures gradually decrease from lunar noon (12:00), reach an inflection point at dusk (18:00) when entering the far side region, and begin rising again at dawn (6:00) upon solar re-exposure. To facilitate the calculation, this study converted lunar local time to the location angle (ζ) between the projection of vector $\vec{n}_1$ onto the equatorial plane and the solar incidence direction, where 12:00, 18:00, and 6:00 correspond to $\zeta = 0$, $\pi/2$, and $3\pi/2$, respectively. The temperature T_{ds} is then fitted as a three-segment 5th-order polynomial function of the angle ζ and latitude (ψ), where $\psi = 0$ corresponds to the equatorial plane. Regarding the calculations of ψ and ζ, the geometric relationships among the angles, vectors, and planes are illustrated in Figure 5 using the special case of $\beta = 0$ as an example for clarity. The final formulation is:

$$T_{ds} = \alpha_0 + \alpha_1\psi + \alpha_2\zeta + \alpha_3\psi^2 + \cdots + \alpha_{19}\psi\zeta^4 + \alpha_{20}\zeta^5 \tag{29}$$

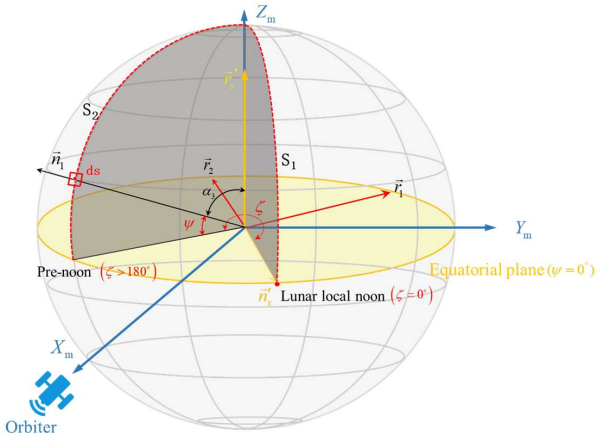


Figure 5. The geometric relationships among angles ψ, ζ, vectors $\vec{r}_1$, $\vec{r}_2$, $\vec{n}'_s$, $\vec{r}'_s$ and planes S_1, S_2.

Table 2 summarizes the coefficients of the polynomial terms, mean squared error (MSE), and coefficient of determination (R^2) for the non-uniform lunar surface temperature fitting. Figure 6 displays the lunar surface temperature contour and its two-dimensional projection generated from the polynomial fitting results.

Table 2. The coefficients of the polynomial terms, mean squared error (MSE), and coefficient of determination (R^2) for the non-uniform lunar surface temperature fitting.

Number	$0<\zeta<1/2\pi$	$1/2\pi<\zeta<3/2\pi$	$3/2\pi<\zeta<2\pi$
0	382.15	517.86	−379,669.39
1	32.80	−74.46	61,402.96
2	40.93	−577.70	313,158.96
3	−66.71	33.56	21,730.75
4	−133.16	87.91	−48,919.99
5	−217.27	322.78	−102,892.53
6	−268.23	−144.26	−2430.28
7	350.06	39.36	−10,892.76
8	143.07	−52.29	14,327.07
9	254.91	−89.09	16,824.01
10	424.05	128.88	1401.50
11	−385.57	−5.53	245.06
12	−74.74	−12.30	1788.28
13	−149.31	13.23	−1839.45
14	−164.25	11.93	−1366.75
15	−184.36	−50.67	−125.20
16	138.14	10.75	−197.68
17	11.95	−3.35	26.39
18	62.09	1.92	−105.30
19	35.38	−1.24	87.74
20	25.57	−0.61	44.05
R^2	0.99845	0.99626	0.99787
MSE	9.898	1.099	12.391

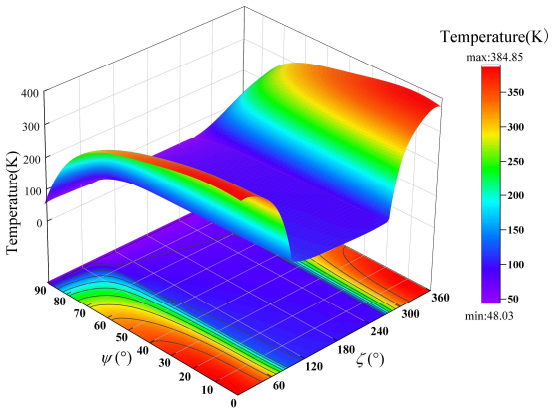


Figure 6. The lunar surface temperature contour and two-dimensional projection.

To computation q_e, the angles ψ and ζ of visible lunar surface elements are first calculated for the orbiter. Then, these parameters are substituted into Equation (29) to determine the temperature T_{ds}, followed by heat flux calculation using Equations (26) and (28). The normal vector of the lunar equatorial plane $\vec{r}_s[0,\ 0,\ 1]_{\mathrm{m}}$ is first defined. After applying the coordinate transformation in Equation (9), the vector is expressed as:

$$\vec{r}_s' = \mathrm{T_{m\text{-}m}}'[0,\ 0,\ 1]_{\mathrm{m}}^{\mathrm{T}} \tag{30}$$

The angle between $\vec{n}_1$ and $\vec{r}_s'$ is calculated using the cosine theorem:

$$\alpha_3 = \arccos\frac{\left|\vec{n}_1 \cdot \vec{r}_s'\right|}{\left|\vec{n}_1\right| \cdot \left|\vec{r}_s'\right|} \tag{31}$$

The latitude ψ is then derived as:

$$\psi = \frac{1}{2}\pi - \alpha_3 \tag{32}$$

To calculate the angle ζ, the plane S_1 is defined by the solar vector $\vec{n}_s'$ and the equatorial $\vec{r}_s'$, with the normal vector:

$$\vec{r}_1 = \vec{r}_s' \times \vec{n}_s' \tag{33}$$

The plane S_2 is defined by the surface element $\vec{n}_1$ and $\vec{r}_s'$, with the normal vector:

$$\vec{r}_2 = \vec{n}_1 \times \vec{r}_s' \tag{34}$$

The result of calculating the angle between vectors $\vec{r}_1$ and $\vec{r}_2$ via the cosine theorem is constrained to the interval $[0,\ \pi]$, but the range of angle ζ is $[0,\ 2\pi]$. Therefore, the expression for ζ requires piecewise processing. Using the direction of the intersection line vector $\vec{r}_s'$ between planes S_1 and S_2 as a reference, the angle ζ is thus defined as:

$$\zeta = \begin{cases} \pi - \arccos\left(\dfrac{\vec{r}_1 \cdot \vec{r}_2}{|\vec{r}_1| \cdot |\vec{r}_2|}\right), & \vec{r}_1 \times \vec{r}_2 \cdot \vec{r}_s' < 0 \\ \pi + \arccos\left(\dfrac{\vec{r}_1 \cdot \vec{r}_2}{|\vec{r}_1| \cdot |\vec{r}_2|}\right), & \vec{r}_1 \times \vec{r}_2 \cdot \vec{r}_s' > 0 \end{cases} \tag{35}$$

3. Discussion

Figure 7 schematically illustrates the projection of the vector $\vec{n}_s'$ onto the orbital plane at $\varphi = 0$ under different i and β, where N_1, N_2, and N_3 represent the intersections of the solar vector with the lunar surface for $\beta = 0$, $0 < \beta < i$, and, respectively. The vectors $\vec{n}_{s1}'$, $\vec{n}_{s2}'$, $\vec{n}_{s3}'$ denote the corresponding projections of the solar vector onto the orbital plane. Key angular relationships are observed at $\varphi = 0$: when $\beta = 0$, the angle between the projection vector of $\vec{n}_s'$ onto the orbital plane ($\vec{n}_s''$ in Figure 7) and the line connecting the lunar center and the orbiter equals $\pi/2$ ($\varphi_0 = \pi/2$); when $\beta = i$, $\varphi_0 = 0$; when $0 < \beta < i$, $\varphi_0 \in (0, \pi/2)$.

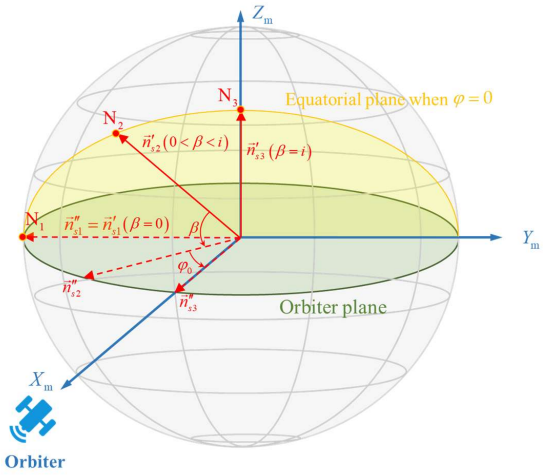


Figure 7. The projection of the solar vector $\vec{n}_s'$ onto the orbiter plane at $\varphi = 0$ under different i and β; φ_0 is the angle between the projection vector of $\vec{n}_s'$ onto the orbital plane ($\vec{n}_s''$) and the line connecting the lunar center and the orbiter.

3.1. Calculation Verification of Infrared View Factor

To validate the effectiveness of the computational methodology and procedures used in this study, the infrared view factor of Earth under typical operational conditions was calculated. The results were compared with theoretical analytical solutions from the Radiative Exchange Factor Handbook [9], as shown in Figure 8. The selected case features a 300 km orbital altitude and the angle between the outer normal vector of the orbiter surface and the line connecting the orbiter to the Earth's center $\delta \in [0^{\circ} \sim 180^{\circ}]$. Comparative analysis demonstrates that the proposed method for determining the infrared view factor between planetary surface elements and the orbiter achieves reliable accuracy, confirming the validity of our computational approach.

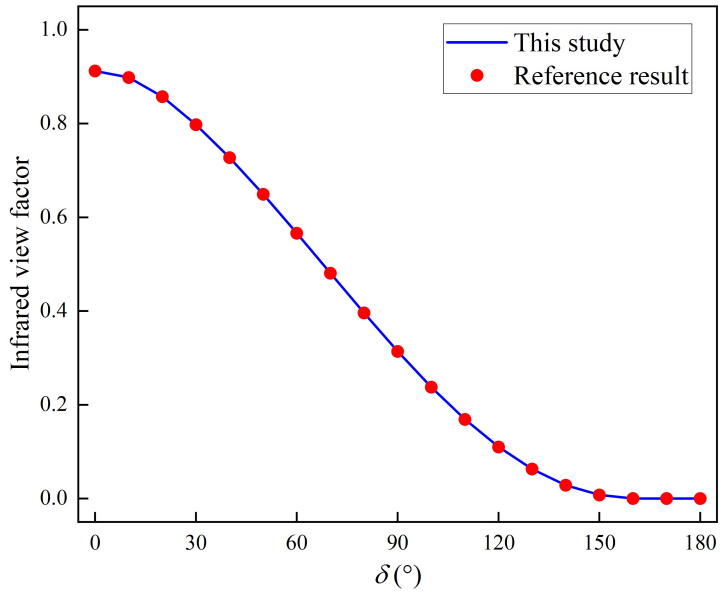


Figure 8. Earth infrared view factor: Comparison of computational results (this study) with Ref. [9] under typical operating conditions.

3.2. Solar Radiation Heat Flux Analysis

Figure 9 shows the two different flight attitudes and the outer normal direction of each surface under the $0 < \beta < \pi/4$ and $\pi/4 < \beta < \pi/2$ condition. The other two attitudes in Table 1 correspond to $-\pi/4 < \beta < 0$ and $-\pi/2 < \beta < -\pi/4$, which is the undrawn part of the equatorial plane in Figure 9. As indicated in Table 1, while the +Z-axis remains unchanged under these attitudes, the +X-axis and +Y-axis are reversed compared to their directions shown in Figure 9. Figure 10 shows the solar radiation heat flux (q_s) from different directions of a hexahedral orbiter under the $\beta = i$ condition. Consequently, φ_{in} and φ_{out} exhibit symmetry relative to $\varphi = 180°$. The range of φ, within which the orbiter resides in the lunar shadow region $(\varphi_s = \varphi_{out} - \varphi_{in})$, varies gradually for $\beta < \pi/4$. When $\beta = 0$, φ_s exceeds $\pi/3$, leading to extended periods of no solar radiation exposure for the orbiter. For the two flight modes, the heat flux q_s from the opposite direction of heat-dissipating surfaces (+Y surface for forward flight mode and +X surface for side flight mode) remains stable throughout the orbital period. The heat flux q_s from +Z direction is most heavily affected by the lunar shadow region, while q_s from $-$Z direction is unaffected by the region. Additionally, q_s from the other two directions exhibit symmetric variations relative to the region with respect to φ, sharing both the rate of change and peak values with the q_s from –Z direction.

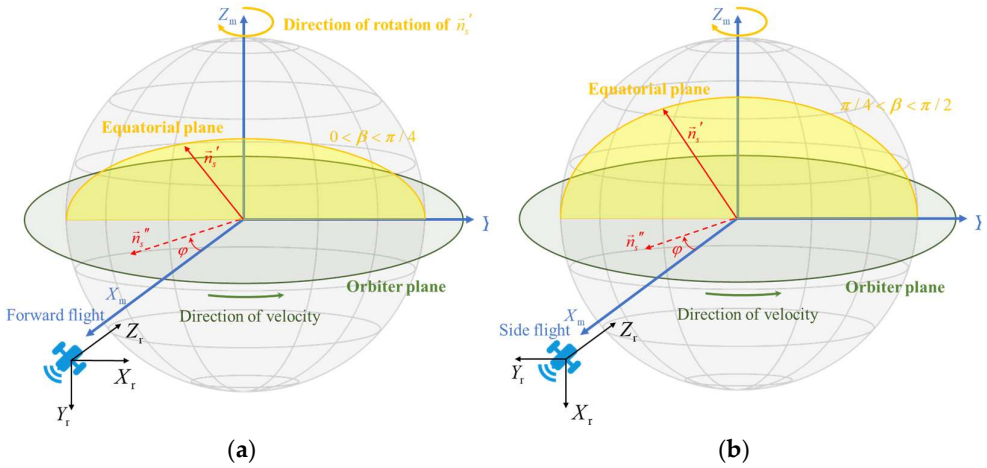


Figure 9. Two different flight attitudes and orientations of the surfaces of the orbiter. (**a**) Forward flight. (**b**) Side flight.

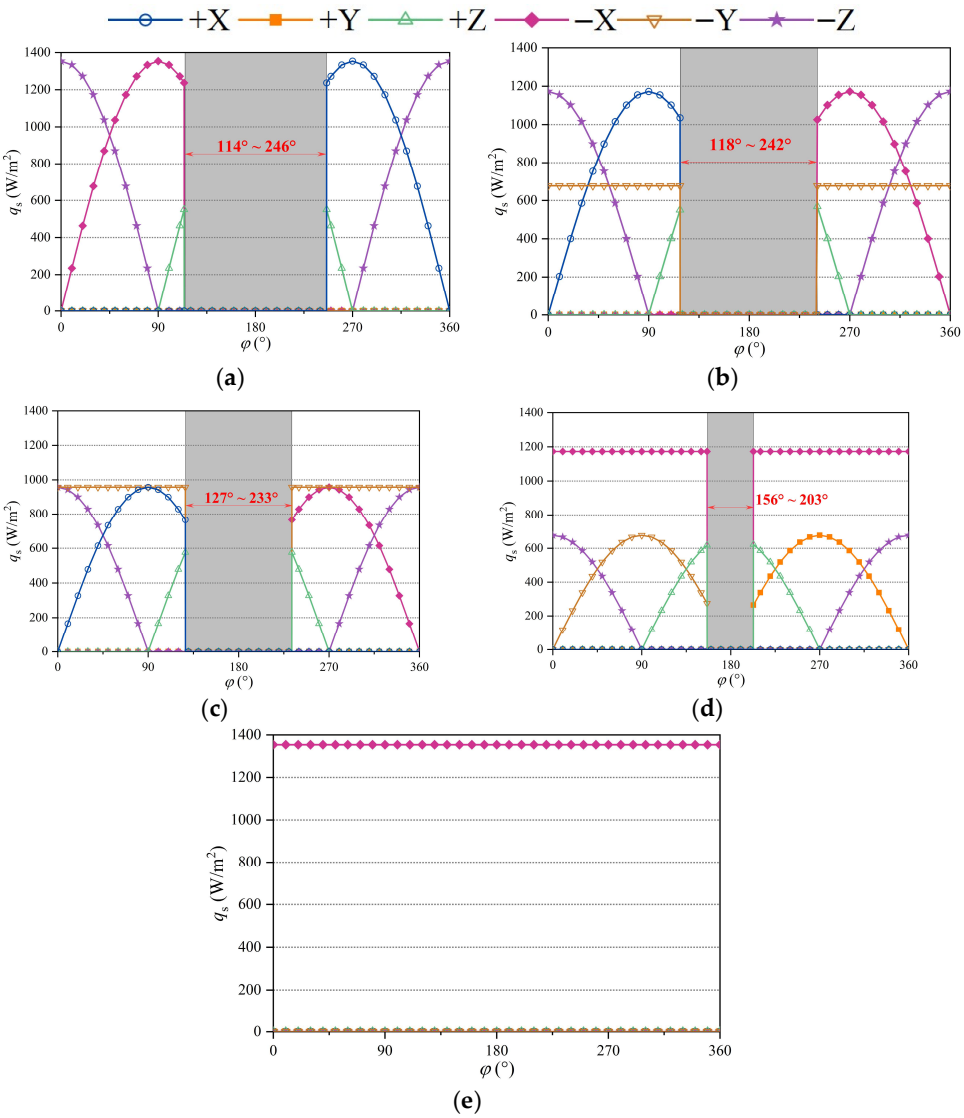


Figure 10. In each direction of a hexahedral spacecraft under the $\beta = i$ condition (**a**) $\beta = 0$. (**b**) $\beta = \pi/6$. (**c**) $\beta = \pi/4$. (**d**) $\beta = \pi/3$. (**e**) $\beta = \pi/2$. The gray areas and the red numbers represent the range of φ where the orbiter is in the lunar shadow region, and the value of φ_{in} and φ_{out}.

Figure 11 presents φ_{in} and φ_{out} under different i and β. For the elliptical orbit, when $\beta \neq 0$, even with identical β, φ_0 and φ_s differ across varying i. Furthermore, when $\beta \neq i$, the symmetry of φ_{in} and φ_{out} relative to $\varphi = 180°$ is no longer preserved. Comparative analysis reveals that φ_s exhibits a monotonic increase with i under constant β. Notably, for $i = \pi/2$, φ_0 remains invariant with β, resulting in slower variations in φ_{in} and an opposite trend in φ_{out} compared to other cases. When $i = \pi/2$ and $\beta \geq 71.17°$, the orbiter does not enter the lunar shadow region during the entire orbital period.

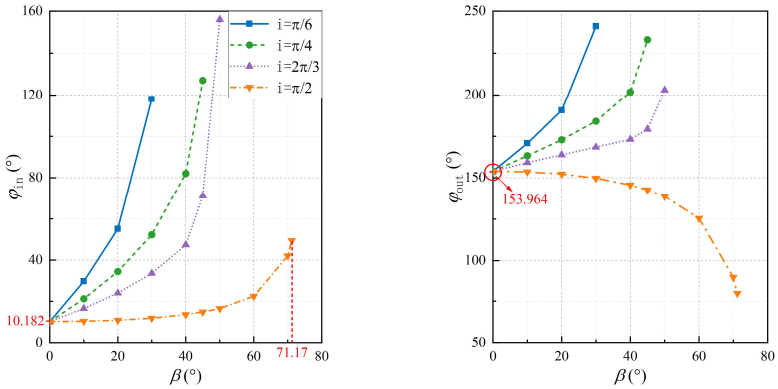


Figure 11. φ_{in} and φ_{out} under different i when $\beta \neq i$. The markers on the ordinate represents $\varphi_{in} = 10.182^{\circ}$ and $\varphi_{out} = 153.964^{\circ}$ when $\beta = 0$.

To systematically analyze the influence of β variation on the q_s under distinct i, numerical results for both +Z and $-$Z directional fluxes at $\beta \neq i$ are obtained, as illustrated in Figure 12. The analysis of q_s variations in the $-$Z direction reveals consistent behavior with the $\beta = i$ scenario, demonstrating that the presence of lunar shadow regions does not significantly influence q_s along this direction. For different i, q_s from $-$Z direction, velocity vector direction, and anti-velocity direction maintain identical variation trends and peak values under equal β conditions when excluding lunar shadow effects, while primarily affecting the range of φ corresponding to $q_s \neq 0$. Notably, elliptical orbital characteristics introduce asymmetric thermal flux distributions in other $q_s \neq 0$ directions. The heat flux in the +Z direction particularly highlights this orbital eccentricity effect, showing significant deviation from the symmetrical heat flux patterns observed in $\beta = i$ or circular orbit scenarios.

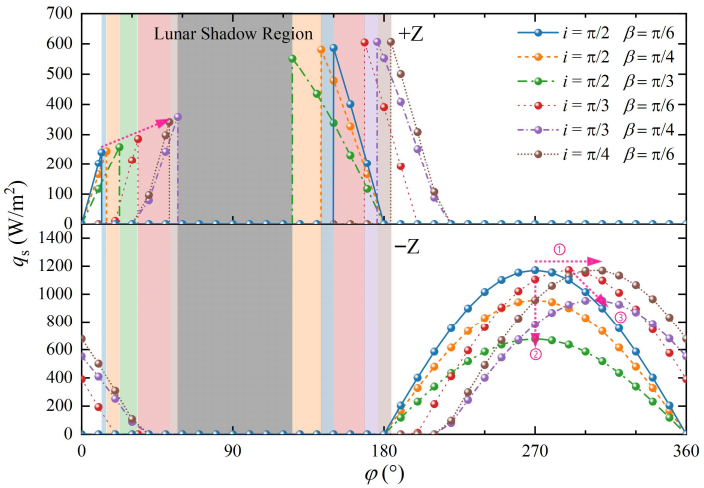


Figure 12. q_s in the +Z and $-$Z directions ($\beta \neq i$) ① i decreases with fixed β; ② β increases for $i = \pi/2$; ③ β increases for $i \neq \pi/2$. The different background colors represent the lunar shadow regions corresponding to the orbit parameters represented by each colored curve.

3.3. Lunar Albedo Heat Flux Analysis

Figure 13 presents the lunar albedo thermal flux (q_r) from six different directions under the $\beta = i$ condition. The thermal flux q_r also demonstrates symmetrical characteristics relative to $\varphi = 180°$, with maximum observed along the +Z direction and $q_r = 0$ along the $-$Z direction consistently, and exhibits comparable magnitudes on the remaining four directions. Moreover, q_r exhibits significant variation with changes in β: the peak reaches 183 W/m^2 when $\beta = 0$, while only on the order of 10^1 W/m^2 when $\beta = \pi/2$.

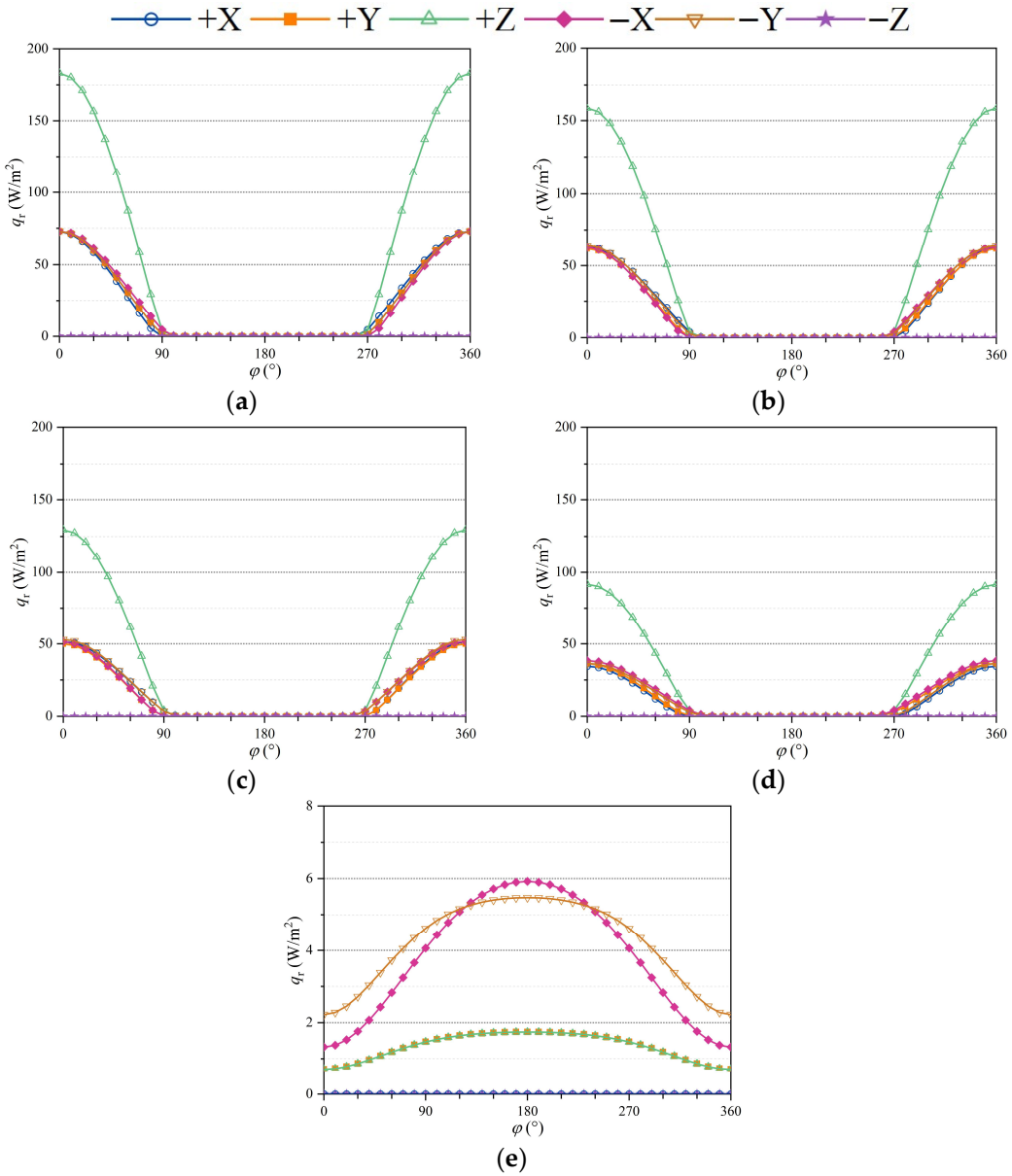


Figure 13. q_r in each direction of a hexahedral spacecraft ($\beta = i$). (**a**) $\beta = 0$. (**b**) $\beta = \pi/6$. (**c**) $\beta = \pi/4$. (**d**) $\beta = \pi/3$. (**e**) $\beta = \pi/2$.

Figure 14 illustrates q_r profiles along the +Z and the velocity direction for $\beta \neq i$ conditions. Analysis reveals an inverse relationship between β magnitude and the peak of q_r during orbital cycles when i remains constant. When $i = \pi/2$ for different cases, with φ_0 fixed at 90°, the variation of β primarily modulates the peak of q_r within the same ranges of φ. In contrast, for $i \neq \pi/2$, increasing β systematically induces rightward shifts and downward displacements of the curves, while simultaneously expanding both the range of φ where $q_r \neq 0$ and the peak of q_r. Furthermore, elliptical orbital dynamics introduce

distinct thermal flux characteristics: (1) Variable L generates i-dependent disparities in peak flux under identical β conditions, particularly pronounced along the velocity vector direction; (2) Asymmetric thermal flux evolution arises from divergent growth and decay rates during orbital cycles, demonstrated by steeper descending slopes contrasted with gradual ascending slopes in the flux profiles.

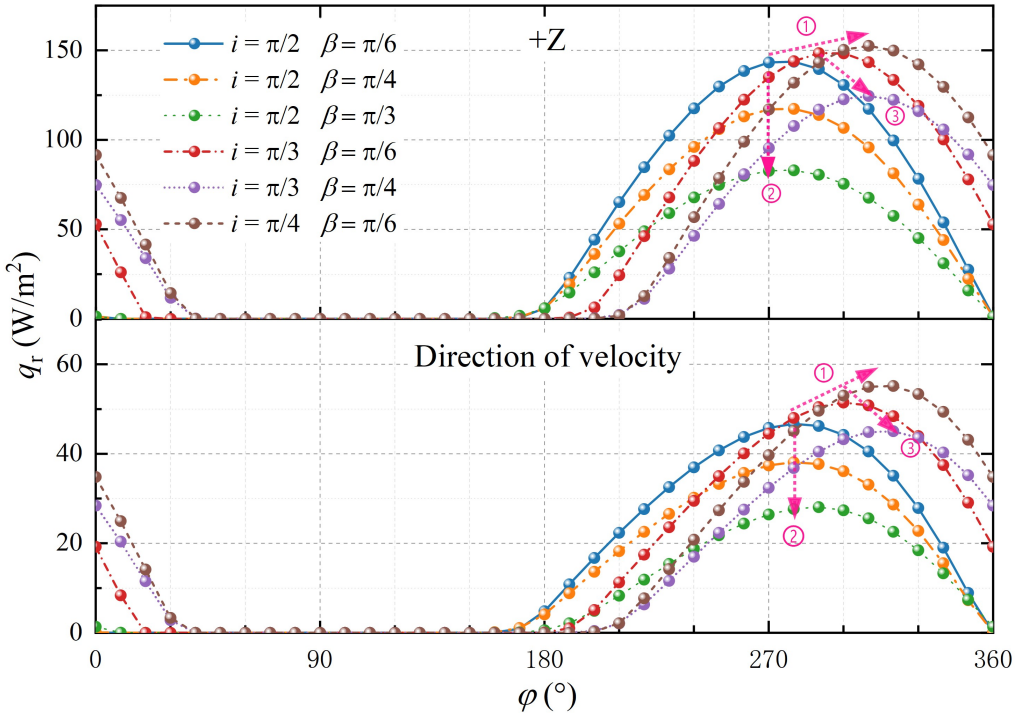


Figure 14. q_r in the +Z and −Z directions under different β ($\beta \neq i$). ① i decreases with fixed β; ② β increases for $i = \pi/2$; ③ β increases for $i \neq \pi/2$.

3.4. Lunar Infrared Radiation Heat Flux Analysis

Figure 15 compares the lunar infrared radiation heat flux q_e in all six directions, calculated by the traditional UPIRM and the NUPIRM under the condition $\beta = i$. The results demonstrate that when considering lunar surface temperature inhomogeneity, the heat flux q_e exhibits significant variations throughout the orbital cycle. Under different β conditions, the maximum q_e reaches 1023 W/m^2, closely aligning with S. Due to the rapid cooling of the lunar surface to approximately 100 K during the lunar night, q_e sharply decreases when the orbiter traverses the lunar night side. Additionally, we calculated the scenario where $\beta = \pi/2$, corresponding to the orbiter remains directly above the boundary between the lunar day and night. In this configuration, the low surface temperatures of the visible lunar terrain combined with the proximity to the fitting boundary induced fluctuations in the computed q_e values. Consequently, only salient features of the results are reported, with the maximum q_e value being approximately 20 W/m^2. In contrast, the uniform radiation model fails to capture these fluctuations, with thermal flux variations across all directions remaining below 100 W/m^2 throughout the cycle. These findings emphasize the necessity of accounting for lunar surface temperature inhomogeneity in orbital thermal analyses to enhance the reliability of thermal control system designs for lunar orbiters.

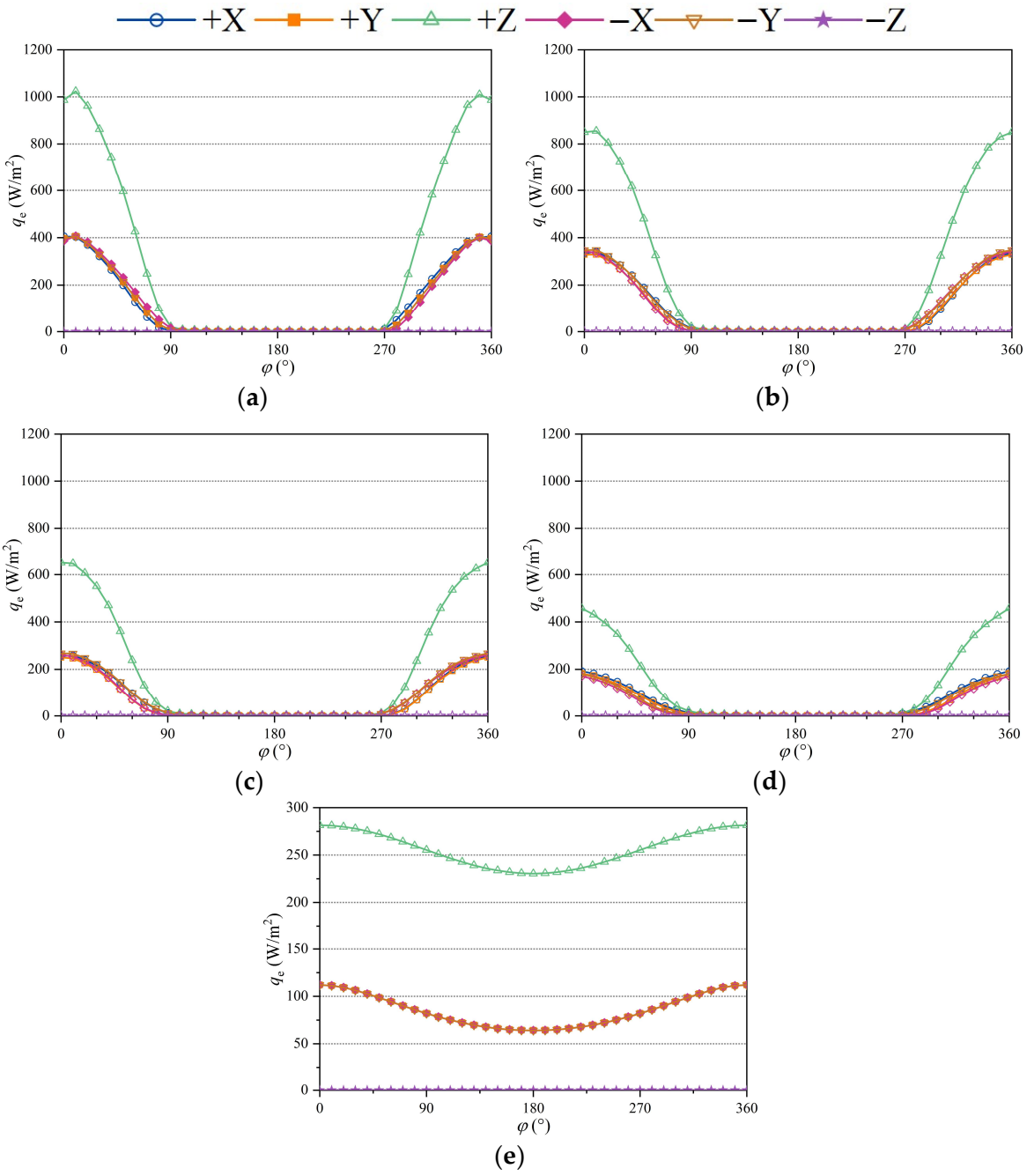


Figure 15. q_e in each direction of a hexahedral spacecraft ($\beta = i$) calculated by (**a**–**d**) NUPIRM; (**e**) UPIRM. (**a**) $\beta = 0$. (**b**) $\beta = \pi/6$. (**c**) $\beta = \pi/4$. (**d**) $\beta = \pi/3$. (**e**) the result of adopting UPIRM.

Figure 16 illustrates the heat flux q_e in the +Z and the velocity direction of the orbiter for $\beta \neq i$. Overall, the influence of varying i and β on q_r and q_e is similar. From the mathematical perspective, this similarity arises because E_{ds} is proportional to the fourth power of T_{ds}, with the high temperature regions near the subsolar point dominating the q_e contribution. As the orbiter approaches the lunar noon region, the value of ψ and η become increasingly similar, while ζ approximately equal to zero. This convergence results in analogous variation trends between heat fluxes q_r and q_e. Physically, ds, which are under stronger solar illumination, absorb and reflect greater thermal flux, resulting in higher local temperatures and enhanced radiative emission. Consequently, the observed similarity in q_r and q_e evolution is consistent with theoretical expectations.

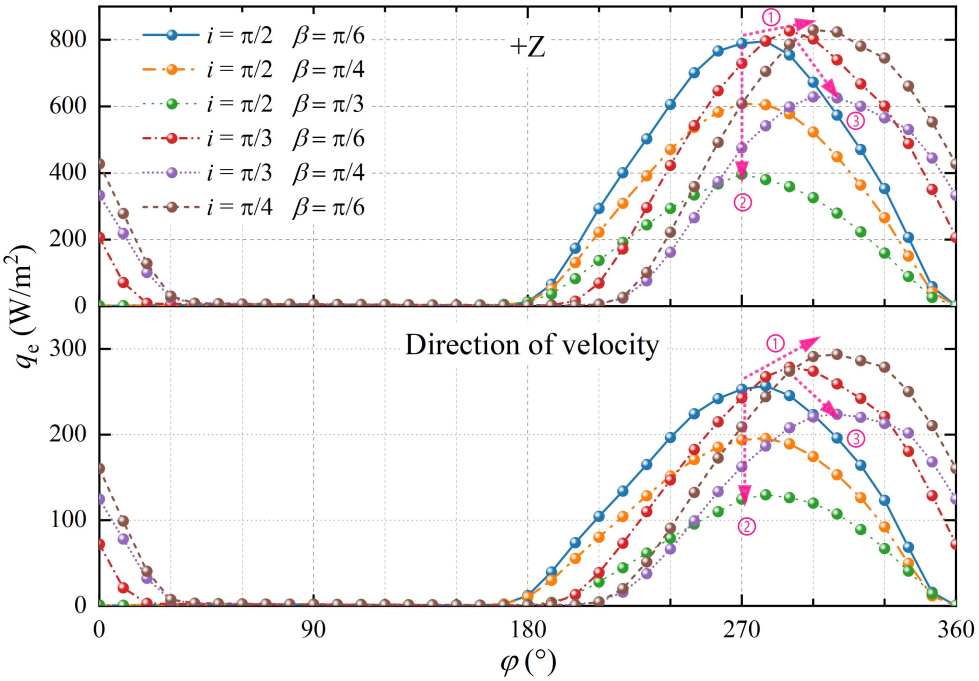


Figure 16. q_e in the +Z and −Z directions under different β ($\beta \neq i$). ① i decreases with fixed β; ② β increases for $i = \pi/2$; ③ β increases for $i \neq \pi/2$.

4. Conclusions

In this study, we developed a method for calculating the external heat flux in different directions of lunar orbiters by adopting the NUPIRM based on the lunar surface temperature data from the LRO Diviner. A coordinate transformation and numerical integration framework was established to quantify the distributions of solar radiation, lunar albedo, and lunar infrared radiation heat flux across the hexahedron spacecraft surfaces under varying β. By analyzing the geometric relationships among β, orbital parameters, and directional vectors, this framework enables the prediction of periodic external heat flux for engineering applications once the variation of β during the orbital cycle is determined.

The NUPIRM incorporates ψ and ζ to fit the lunar surface temperature distribution, accounting for extreme variations from 120 °C to −170 °C. The three-segment polynomial regression achieved MSE of 9.898, 1.099, and 12.391 in different segments. The results demonstrate that the NUPIRM can capture significant infrared radiation flux fluctuations, ranging from 1023 W/m^2 to 20 W/m^2 under the orbital parameters in this study. Comparative analysis highlights the necessity of adopting the NUPIRM over the UPIRM. Additionally, the trends of the heat flux under varying β were systematically characterized.

The limitations include the assumption of static lunar surface temperatures and the exclusion of transient effects. Future work should integrate dynamic temperature evolution and validate predictions with in situ measurements. Nevertheless, this study provides a foundational framework for optimizing thermal control strategies in lunar and deep-space missions.

Author Contributions: Conceptualization, X.L. and X.Q.; methodology, X.L. and X.Q.; software, X.L.; validation, X.L. and X.Q.; formal analysis, X.L.; investigation, X.L.; resources, L.T., J.M., X.Q. and X.L.; data curation, X.L. and X.Q.; writing—original draft preparation, X.L.; writing—review and editing, L.T., J.M. and X.Q.; visualization, X.L.; supervision, L.T., J.M. and X.Q.; project administration, X.L.; funding acquisition, L.T. All authors have read and agreed to the published version of the manuscript.

Funding: This research received no external funding.

Data Availability Statement: The data presented in this study are available upon request from the corresponding author.

Conflicts of Interest: The authors declare no conflicts of interest.

Abbreviations

UPIRM	Uniform planetary infrared radiation model
LRO	Lunar Reconnaissance Orbiter
NUPIRM	Non-uniform planetary infrared radiation model
LLCD	Lunar Laser Communication Demonstration
MSE	Mean squared error

References

1. Meseguer, J.; Pérez-Grande, I.; Sanz-Andrés, A. *Spacecraft Thermal Control*; Elsevier: Philadelphia, PA, USA, 2012; pp. 15–38.
2. Lv, Y.G.; Wang, Y.T.; Meng, T.; Wang, Q.W.; Chu, W.X. Review on thermal management technologies for electronics in spacecraft environment. *Energy Storage Sav.* **2024**, *3*, 153–189. [CrossRef]
3. Shin, S.; Lim, J.H.; Kim, C.G. Thermal parameter determination in underdetermined spacecraft thermal models using surrogate modeling. *Acta Astronaut.* **2024**, *214*, 583–592. [CrossRef]
4. Cui, Q.; Lin, G.; Cao, D.; Zhang, Z.; Huang, Y. Thermal design parameters analysis and model updating using Kriging model for space instruments. *Int. J. Therm. Sci.* **2022**, *171*, 107239. [CrossRef]
5. Xiong, Y.; Guo, L.; Yang, Y.T.; Wang, H.L. Intelligent sensitivity analysis framework based on machine learning for spacecraft thermal design. *Aerosp. Sci. Technol.* **2021**, *118*, 106927. [CrossRef]
6. Huang, H.Z.; Bu, C.G. Thermal Design and Experimental Validation of a Lightweight Microsatellite. *Aerospace* **2025**, *12*, 52–66. [CrossRef]
7. De Zanet, G.; Viquerat, A.; Aglietti, G. Predicted thermal response of a deployable high-strain composite telescope in low-Earth orbit. *Acta Astronaut.* **2023**, *205*, 127–143. [CrossRef]
8. Yi, H.; Huang, X.; Jiang, H. Common Calculation Method for Orbital Heat Flux of Spacecraft on Circular Orbit. *Spacecr. Eng.* **2021**, *30*, 53–58. [CrossRef]
9. Li, P.; Zhao, J.Z.; Lai, X.Y.; Li, Z.G. Investigation of an Accurate Calculation Method for Moon Infrared Radiation on Target Surface in Lunar Orbit. *Aerosp. Shanghai* **2015**, *32*, 31–41. [CrossRef]
10. Mermer, E.; Ünal, R. A novel entropy calculation approach for sensor placement optimization for a satellite thermal control system. *Measurement* **2025**, *249*, 116963. [CrossRef]
11. Selvadurai, S.; Chandran, A.; Valentini, D.; Lamprecht, B. Passive Thermal Control Design Methods, Analysis, Comparison, and Evaluation for Micro and Nanosatellites Carrying Infrared Imager. *Appl. Sci.* **2022**, *12*, 2858. [CrossRef]
12. Garzón, A.; Tami, J.A.; Campos-Julca, C.D.; Acero-Niño, I.F. Effect of beta angle and contact conductances on the temperature distribution of a 3U CubeSat. *Therm. Sci. Eng. Prog.* **2022**, *29*, 101183. [CrossRef]
13. Wang, L.Y.; Zhu, H.; Xu, W.; Meng, N.Y. Thermal-structural analysis of a large space hoop-column antenna under unidirectional solar radiations. *Thin-Walled Struct.* **2024**, *198*, 111695. [CrossRef]
14. Li, S.; Jiang, X.Q.; Tao, T. Guidance Summary and Assessment of the Chang'e-3 Powered Descent and Landing. *J. Spacecr. Rocket.* **2016**, *53*, 258–277. [CrossRef]
15. Xiao, X.; Yu, S.R.; Huang, J.; Zhang, H.; Zhang, Y.W.; Xiao, L. Thermophysical properties of the regolith on the lunar far side revealed by the in situ temperature probing of the Chang'E-4 mission. *Natl Sci Rev* **2022**, *9*, 175–184. [CrossRef] [PubMed]
16. Pettit, E.; Nicholson, S.B. Lunar radiation and temperatures. *Astrophys. J.* **1930**, *71*, 102–135. [CrossRef]
17. Chin, G. Lunar Reconnaissance Orbiter: Mission Overview. In Proceedings of the 36th COSPAR Scientific Assembly, Beijing, China, 16–23 July 2006; p. 668.
18. Hayne, P.O.; Bandfield, J.L.; Siegler, M.A.; Vasavada, A.R.; Ghent, R.R.; Williams, J.P.; Greenhagen, B.T.; Aharonson, O.; Elder, C.M.; Lucey, P.G.; et al. Global Regolith Thermophysical Properties of the Moon From the Diviner Lunar Radiometer Experiment. *J. Geophys. Res. Planets* **2017**, *122*, 2371–2400. [CrossRef]
19. Gan, H.; Zhao, C.X.; Wei, G.F.; Li, X.Y.; Xia, G.J.; Zhang, X.; Shi, J.J. Numerical Simulation of the Lunar Polar Environment: Implications for Rover Exploration Challenge. *Aerospace* **2023**, *10*, 598–612. [CrossRef]
20. Yin, Z.L.; Liu, N.T.; Jin, Y.Q. Simulation of the temperatures in the permanently shadowed region of the Moon's south pole and data validation. *Icarus* **2024**, *411*, 115917. [CrossRef]
21. Boroson, D.M.; Robinson, B.S.; Murphy, D.V.; Burianek, D.A.; Khatri, F.; Kovalik, J.M.; Sodnik, Z.; Cornwell, D.M. Overview and results of the Lunar Laser Communication Demonstration. *Proc. SPIE* **2014**, *8971*, 213–223. [CrossRef]

22. Ping, J.S. Thermal environmental effect on the Chang'E-5 lander revealed by in-situ temperature data. *Sci. China Phys. Mech. Astron.* **2023**, *66*, 22–36. [CrossRef]
23. Ma, Y.; Zhang, S.; Liu, Y.; Ma, C. Lunar long-wave infrared radiation characteristics based on space based quantitative measured data. *Chin. Opt.* **2022**, *15*, 525–533. [CrossRef]

Disclaimer/Publisher's Note: The statements, opinions and data contained in all publications are solely those of the individual author(s) and contributor(s) and not of MDPI and/or the editor(s). MDPI and/or the editor(s) disclaim responsibility for any injury to people or property resulting from any ideas, methods, instructions or products referred to in the content.